Chapter 6 $Ca(Fe_{1/2}Nb_{1/2})O_3$ as an incipient antiferromagnet: Role of critical percolation threshold concentration

6.1. Introduction

Magnetoelectric multiferroic materials, in which ferroelectric and magnetic orders not only coexist but also couple with each other, have received enormous attention in the current research [29,31,32,68,95]. Such materials have great promises for the development of new multifunctional devices for technological applications like sensors, actuators, storage devices, spintronics etc [29,32,34,68]. It has been shown that the ferroelectricity in ABO_3 perovskites arises due to the off-centring of the B-site cation which requires empty d-orbitals (d^0) [37] while the magnetism requires partially filled d orbitals (d^n). Since the two conditions are mutually exclusive the magnetoelectric multiferroics were believed to be rare [38]. The last two decades have witnessed the discovery of new multiferroic compounds like $RMnO_3$ (R = Tb, Dy, Y), $MnWO_4$, $LiCu_2O_2$, $Ni_3V_2O_8$, $LiCuVO_4$, $CoCrO_4$, CuO, $Ba_2Mg_2Fe_{12}O_{22}$, $Ba_{0.5}Sr_{1.5}Zn_2Fe_{12}O_{22}$ etc. in which polarization is induced as a result of magnetic order through inverse D-M interaction [39,40,315,316]. In such multiferroics, the mutually exclusiveness due to d^0 and d^n requirement is avoided, since ferroelectric polarization is an off-shoot of the magnetic transition itself coming from d^n element. The magnetic transition temperature in these materials is well below the room temperature. Unlike these multiferroics where ferroelectric polarization is a secondary order parameter where as the primary order parameter is magnetization, nature has also provided materials like $BiFeO_3$ where ferroelectricity originates from the hybridization of the $6s^2$ orbital of Bi^{3+}-ion containing stereochemically active lone pair of electrons with 2p orbitals of O^{2-}, while magnetism results from the $3d^5$ electrons of Fe^{3+} ion. This compound shows ferroelectric and antiferromagnetic transition temperatures as T_C ~1103K and T_N ~650K,

respectively [68,95]. In such materials, both ferroelectric polarization (P) and magnetization (M) are primary order parameters which emerge below T_C and T_N and also couple with each other [89,90,94]. Such multiferroics are termed as type-I whereas the former are termed as type-II multiferroics. In general, type-I multiferroics exhibit large ferroelectric polarization (~100μC/cm^2 for $BiFeO_3$) but weak magnetoelectric coupling whereas type-II multiferroics result in weak ferroelectric polarization ($\leq 10^{-2}$μC/cm^2) but strong magnetoelectric coupling [39,40,315,316].

Nearly six decades back, Russian researchers adopted another strategy to produce type-I multiferroicity by substituting both magnetic transition metal ion with d^n electrons like Fe, Co, Ni etc and ferro-active transition metal ions with d^0 electronic configuration, such as Nb^{5+}, Ta^{5+}, W^{6+} [147,152,171,172,174,191,192], at the B-site of the ABO_3 perovskite structure [183,184]. Using this idea, multiferroicity was reported in B-site disordered compounds like $Pb(Fe_{1/2}Nb_{1/2})O_3$ (PFN), $Pb(Fe_{1/2}Ta_{1/2})O_3$ (PFT) and $Pb(Fe_{2/3}W_{1/3})O_3$ (PFW) [147,152,171,172,174,183,184,191,192]. The d^0-ness of the Nb^{5+}, $Ta^{5+}$and W^{6+} and $6s^2$ lone pair of Pb^{2+} are believed to facilitate the development of ferroelectric order through hybridization of $4d^0$ Nb^{5+}, $5d^0$ Ta^{5+}, $5d^0$ W^{6+} and $6s^2$ Pb^{2+} orbitals with $2pO^{2-}$ orbitals [37,38]. One of the biggest puzzles about such complex perovskites is that only the Pb-based compounds PFN, PFT, and PFW show the expected long-range ordered (LRO) ferroelectric (FE)/ relaxor FE behaviour below T_C and also LRO AFM transition at T_N, whereas the corresponding Pb-free compounds like $Ca(Fe_{1/2}Nb_{1/2})O_3$ (CFN), $Sr(Fe_{1/2}Nb_{1/2})O_3$ (SFN), $Ba(Fe_{1/2}Nb_{1/2})O_3$ (BFN), $Ca(Fe_{1/2}Ta_{1/2})O_3$ (CFT), $Sr(Fe_{1/2}Ta_{1/2})O_3$ (SFT), $Ba(Fe_{1/2}Ta_{1/2})O_3$ (BFT) neither show LRO FE/relaxor FE nor LRO AFM transition [176–178]. The only common feature in both group of compounds is that they exhibit spin-glass (SG) transition in the range 10-25K. In the preceding chapter, we discussed at length the role of short range ordered AFM spin

clusters in the spin glass phase of these compounds taking CFN as an example. In this chapter, we address the issue of absence of LRO AFM in Pb-free disordered compounds of the type $A(Fe_{1/2}B_{1/2})O_3$ taking $Ca(Fe_{1/2}Nb_{1/2})O_3$ (CFN) and its solid solutions with $BiFeO_3$ (BF) and $LaFeO_3$ (LF) as examples.

Raeviskii et al. [203] proposed that the stability of the LRO AFM phase is significantly enhanced in Pb-based compounds as compared to Pb-free compounds due to the critical role of lone pair electrons of $6s^2Pb^{2+}$ orbital. They proposed that in these compounds, the superexchange interactions can also be mediated by Pb^{2+} (Fe^{3+}-Pb^{2+}-Fe^{3+}) in the $<111>_{pc}$ direction to form the LRO AFM phase in contrast to Pb-free perovskite compounds where the superexchange interaction is via oxygen only, i.e. Fe^{3+}-O^{2-}-Fe^{3+} [194]. Theoretically, the stabilisation of LRO magnetic phase in disordered Ising and Heisenberg systems is decided by the percolation threshold concentration (c_p) [24,195–197]. The percolation threshold value is highly sensitive to the strength of the exchange interactions and therefore varies from material to material [238,239,242,243]. Monte-Carlo calculations for 3D Heisenberg systems with simple cubic lattice have predicted a percolation threshold (c_p) value of ~0.307 [195–197] while for the 3D Ising system this value is ~0.88 [195]. Since some of the Pb-free complex perovskites like CFN and SFN have tilted octahedral configuration, which makes the Fe^{3+}-O^{2-}-Fe^{3+} bond angles deviate from 180°, in marked contrast to the paraelectric/paramagnetic phase of the Pb-based PFN, PFT and PFW. Such a bending of Fe^{3+}-O^{2-}-Fe^{3+} bonds would make Dzyaloshinskii-Moriya (D-M) interaction non zero and lead to spin canting [317]. This makes the systems like CFN effectively Heisenberg type. Since the concentration of magnetic ion (Fe^{3+}) on the B-site of the CFN is 50%, which is considerably higher than the percolation threshold limit for 3D Heisenberg systems, it is surprising that such Pb-free complex perovskites do not show any transition to a LRO AFM phase. Theoretical models have

predicted a LRO AFM transition around 200K in such systems [318] but the transition does not happen in real systems. Therefore, it is of interest to verify if the absence of the LRO AFM phase could be due to the percolation threshold problem in such Pb free complex perovskites.

With this objective in mind, we present in this chapter the results of dc magnetization neutron scattering and dielectric measurements on CFN and its solid solutions. Our neutron diffraction results reveal that CFN is an incipient AFM whose SRO AFM correlation length start growing below 200K eventhough the size of the AFM spin-clusters remains limited to ~2 nm at the lowest temperature (4K). We also show that the LRO AFM state of CFN can be stabilized with T_N~175K by increasing the Fe^{3+} content slightly by about 5% through a solid solution formation with compounds like $BiFeO_3$ and $LaFeO_3$. Observation of significant magnetoelastic and magnetodielectric coupling in the vicinity of T_N in these solid solutions, raises the possibility of CFN being a multiferroic.

6.2. Sample preparation:

Polycrystalline $Ca(Fe_{1/2}Nb_{1/2})O_3$ (CFN), and $0.90Ca(Fe_{1/2}Nb_{1/2})O_3$-$0.10BiFeO_3$ (CFN-0.10BF), $0.90Ca(Fe_{1/2}Nb_{1/2})O_3$-$0.10LaFeO_3$ (CFN-0.10LF) were prepared by standard solid-state thermochemical route using high purity carbonates ($CaCO_3$), and oxides (Bi_2O_3, Fe_2O_3, La_2O_3, and Nb_2O_5) supplied by Sigma Aldrich. The details of sample preparation of CFN is given in the preceding chapter. We followed the same procedure for the preparation of CFN-0.10BF and CFN-0.10LF solid solution samples also. Here, we would like to mention that the sintering of the CFN-0.10BF was carried out in a closed alumina crucible with calcined powder of the same composition as spacer powder for preventing the loss of Bi_2O_3 during sintering. CFN-0.10LF was, on the otherhand, sintered in an open crucible.

6.3. Characterizations:

The characterization of CFN is already given in the previous chapter. Microstructure of the CFN-0.10BF pellet was obtained using a Carl-Zeiss Scanning Electron Microscope (SEM), model no. EVO 18. The chemical compositions were checked by Energy Dispersive X-ray spectroscopy (EDX) attachment (Oxford, model no. 51-ADD0048) in the above-mentioned SEM. The sintered pellet was coated with conducting gold using sputter coater (Royal life Sciences, model no. DSR1) under vacuum before taking the SEM images.

X-ray powder diffraction (XRD) measurements were carried out on CFN-0.10BF and CFN-0.10LF using an 18-kW Cu rotating anode powder diffractometer (Rigaku, model no. RINT 2500/PC series) operating in the Bragg-Brentano geometry and fitted with a curved crystal monochromator in the diffraction beam. The data were collected in the 2θ range 20 to 120° at a step of 0.02 degrees.

High-resolution neutron powder diffraction (NPD) patterns were collected on CFN in the temperature range 4-300K at close temperature intervals using structure powder diffractometer SPODI at FRM-II research reactor in Garching, Germany. The incident neutron wavelength was 1.5482Å as obtained from germanium (551) reflection of vertically focussed monochromator at a take-off angle of 155°. Approximately 12g powder sample was kept in a cylindrical vanadium (V) can of diameter 4mm which was cooled to different temperatures using close cycle helium refrigerator. The temperature dependent NPD data on CFN-0.10BF and CFN-0.10LF samples were collected in the range 290 K to 3 K at Druva reactor, BARC, Mumbai at a wavelength of 1.48 Å using high-resolution powder diffractometer PD-3 over 2θ =5 to 120 degrees. A close cycle helium refrigerator (CCR) (Cryogenic, A S Scientific UK) with variable temperature insert (VTI) was used for sample temperature variation. For this also, the powder sample

was filled in a vanadium can of 6mm diameter and attached to the sample rod of the VTI. The nuclear and magnetic structures were analysed by Rietveld technique using FullProf suite [253].

DC magnetization measurements were carried out on vibrating sample magnetometer (VSM) option attached to physical property measurement system (Dynacool PPMS, Quantum Design).

For the dielectric measurements, the pellets were gently polished with 0.25μm size diamond paste. After then acetone was used to clean the surfaces and then put on the isopropyl alcohol to remove the moisture on the surfaces. The electroding of the pellets on both sides was done using fired-on silver paste which is cured at 773K for 5 minutes. Low temperature dielectric measurement was performed at a heating rate of 1K/minute using a fully computer-controlled measuring system involving Novocontrol (Alpha-A) high performance frequency analyzer and 7T cryogen free superconducting magnet-based measurement system (Cryogenic, model no. 7 Tesla mini CFM).

6.4. Results and discussion:

6.4.1 Microstructure and chemical composition:

The details of microstructure and chemical composition of $Ca(Fe_{1/2}Nb_{1/2})O_3$ are already given in the previous chapter V. A typical scanning electron micrograph image of ceramic sample of CFN-0.10BF is shown in Fig. 6.1(a). The average grain size was estimated using Image J software and is found to be approximately (2.8±0.3) μm. The EDX spectrum of CFN-0.10BF sample shown on the right panel (b) of Fig.6.1 reveals that the ceramic sample consists of calcium (Ca), iron (Fe), niobium (Nb), bismuth (Bi), and oxygen (O) atoms. The EDX analyses were carried out at several randomly selected regions and the results of the average composition is given in Table 6.1. It is evident from these table that the average composition obtained by EDX analysis is close to the nominal

(expected) composition within the limit of standard deviation for Ca, Fe, Nb, Bi, and O. This confirms the excellent quality of the sample. We expect CFN-0.10LF sample to be of the same quality.

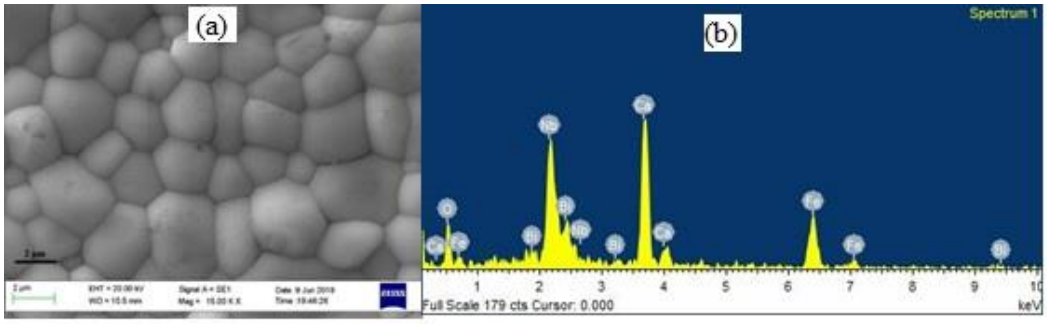

Figure 6.1: **(a)** Microstructure and **(b)** EDX spectra of CFN-0.10BF ceramic sample.

Table 6.1: Quantification of chemical composition of CFN-0.10BF sample.

Elements	Average chemical composition in wt %	
	Expected	Observed
Ca	20.3	19.9 ± 0.8
Bi	11.8	11.7 ± 0.9
Fe	17.3	16.7 ± 0.8
Nb	23.6	24.9 ± 0.8
O	27.0	26.8 ± 0.7

6.4.2 Room temperature crystal structure:

The room temperature crystal structure of CFN has already been discussed in chapter V. In CFN samples, we observed three types of superlattice reflections having indices odd-odd-odd (ooo), odd-odd-even (ooe) and even-even-odd (eeo). The presence of ooo and ooe type superlattice reflections confirms the anti-phase and in-phase tilts in these compounds. The superlattice reflections with indices of eeo-type arise due to the

antiparallel cation displacement of the A-site cation. Such superlattice reflections are also observed similar to that for the well-known perovskite compound $CaTiO_3$ which belongs to $a^-a^-c^+$ tilt system in Glazer's notation [204] with orthorhombic structure in the Pbnm space group. In the previous chapter, we confirmed this structure for CFN. Since diffraction peaks of CFN-0.10BF and CFN-0.10LF are identical to CFN with no extra peaks or additional peak splitting, we expect the orthorhombic structure in the Pbnm space group for these solid solutions of CFN also. The room temperature crystal structure of CFN-0.10BF and CFN-0.10LF was further confirmed by Rietveld refinement using XRD data. As for the asymmetric unit of orthorhombic phase of CFN-0.10BF and CFN-0.10LF is concerned, the Ca/Bi/La occupy 4c Wyckoff site at (x, y, 1/4) position, Fe/Nb occupy 4b Wyckoff site at (1/2, 0, 0) position. The two oxygen atoms O_1 occupy the Wyckoff 4c and 8d sites with positional coordinates (x, y, 1/4) and (x, y, *z*), respectively. We used linear interpolation and pseudo-Voigt function for modelling of the background and peak shape. During the refinement, the occupancy of all the atoms was fixed to the nominal composition and all other parameters like zero correction, scale factor, background, lattice parameters, half width parameters (u, v and w), positional coordinates and thermal parameters were varied. The refinements converged after a few cycles. Fig. 6.2 compares the results of the Rietveld refinement of CFN, CFN-0.10BF and CFN-0.10LF at room temperature. The observed (filled-circles) and calculated (continuous line) profiles show excellent fit as can be seen from the nearly flat difference (bottom line) profile. This confirm that all the three compounds belong to orthorhombic crystal structure in the Pbnm space group with $a^-a^-c^+$ tilt system. The refined unit cell parameters, positional coordinate and thermal parameters are given in Table 6.2.

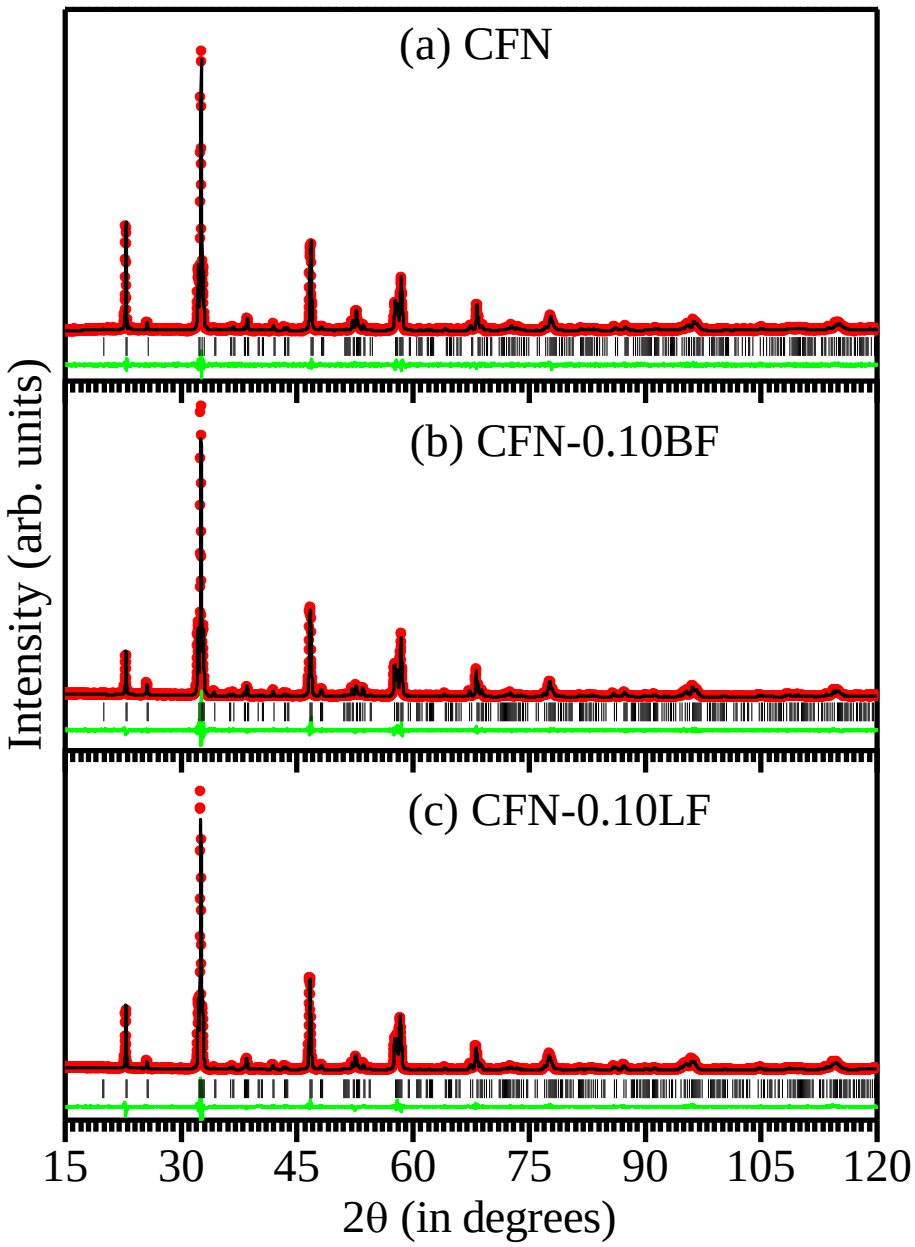

Figure 6.2: Observed (red dots), calculated (black continuous line) and difference (green continuous line) profiles obtained from Rietveld refinement using x-ray diffraction data of **(a)** $Ca(Fe_{1/2}Nb_{1/2})O_3$ **(b)** $Ca(Fe_{1/2}Nb_{1/2})O_3$-0.10$BiFeO_3$ **(c)** $Ca(Fe_{1/2}Nb_{1/2})O_3$-0.10$LaFeO_3$ at room temperature using Pbnm space group. Vertical tick marks above the difference profile represent the Bragg peak positions.

Table 6.2: Rietveld refined structural parameters and agreement factors for CFN, CFN-0.10BF and CFN-0.10LF using Lab XRD data at 300K with Pbnm space group.

Parameters	CFN	CFN-0.10BF	CFN-0.10LF
$A_{O\,(Å)}$	5.4455 (1)	5.4499 (1)	5.4609 (2)
$B_{O\,(Å}$	5.5501 (2)	5.5613 (9)	5.5531 (2)
$C_{O\,(Å}$	7.7556 (2)	7.7669 (1)	7.7727 (1)
$V_{O\,(Å^3)}$	234.398 (11)	235.413 (7)	235.710 (12)
α, β, γ	$\alpha=\beta=\gamma=90^0$	$\alpha=\beta=\gamma=90^0$	$\alpha=\beta=\gamma=90^0$
Ca/Bi (x)	0.010 (1)	0.006 (7)	0.006 (7)
Ca/Bi (y)	0.042 (5)	0.046 (3)	0.038 (3)
Ca/Bi (z)	0.25	0.25	0.25
Fe/Nb (x)	0.5	0.5	0.5
Fe/Nb (y)	0	0	0
Fe/Nb (z)	0	0	0
O1 (x)	0.9194 (2)	0.9155 (1)	0.9128 (2)
O1 (y)	0.4476 (2)	0.4802 (1)	0.473 (1)
O1 (z)	0.25	0.25	0.25
O2 (x)	0.2995 (1)	0.2894 (1)	0.2932 (9)
O2 (y)	0.2922 (1)	0.2937 (9)	0.2987 (8)
O2 (z)	0.0436 (9)	0.0461 (8)	0.045 (8)
$\beta_{Ca/Bi}$ (Å^2)	1.05 (6)	1.21 (4)	1.21 (4)
$\beta_{Fe/Nb}$ (Å^2)	0.51 (4)	0.51 (2)	0.51 (2)
β_{O1} (Å^2)	1.43 (2)	0.36 (1)	0.36 (1)
β_{O2} (Å^2)	0.75 (2)	0.34 (2)	0.34 (2)
R_{wp} (%)	17.3	18.3	18.8
χ^2	1.43	1.46	1.51

6.4.3 Magnetic transitions in CFN, CFN-0.10BF and CFN-0.10LF:

6.4.3.1 DC magnetization studies:

Fig. 6.3 depicts the temperature dependence of dc magnetization M(T) of CFN, CFN-0.10BF and CFN-0.10LF samples measured in the temperature range 2-395K at 500 Oe field during heating cycle after zero-field cooled (ZFC) and field cooled (FC) conditions of the sample. It is evident from Fig. 6.3(a) that the ZFC curve for CFN gradually increases with decreasing temperature from 395K and reveals a cusp at 25K due to spin-glass transition discussed in the previous chapter and a kink around 10K of unknown origin. While the ZFC M(T) curve of CFN-0.10BF and CFN-0.10LF also increases gradually upto around 175K (see Figs. 6.3(c) and (e)) but it begins to increase sharply below 175K revealing the occurrence of a LRO magnetic transition. On further

cooling, the ZFC M(T) shows two anomalies around 50K and 16K. We believe that as a result of substitution of 10%$BiFeO_3$ or 10%$LaFeO_3$ in CFN, the low temperature transitions at 25K and 10K of CFN have shifted towards higher temperature side. What is most significant is the appearance of a new magnetic transition around 175K which is not seen in the case of pure CFN. This indicates that the CFN is at the verge of acquiring LRO state and increasing the Fe^{3+} content slightly from 50% to 55% led to the stabilization of the LRO state, presumably as a result of crossing the percolation threshold value.

In order to check what type of LRO correlation is developing below 175K in these two solid solutions, we plot the temperature dependence of inverse of ZFC magnetic susceptibility (see Figs. 6.3(b) (d) and (f)). A least-squares fit using Curie-Weiss (C-W) law $\chi(T) = \left(\frac{C}{T-\theta_W}\right)$ above 350K yields Curie constant C = 1.241, 1.254, and 1.293 emuK $mol^{-1}Oe^{-1}$ and Curie-Weiss temperature θ_W = -(113.7±0.8), -(137.9±1) and –(131.8±5)K for CFN, CFN-0.10BF, CFN-0.10LF, respectively. The effective magnetic moment (μ_{eff}) determined from Curie constant using relationship $\mu_{eff} = 3Ck_B/N_A$ comes out to be 3.15, 3.18 and 3.22μ_B for the three compositions. The large negative value of Curie-Weiss temperature confirms the presence of strong antiferromagnetic correlations in CFN. It also confirms that the LRO state of the two solid solutions corresponds to AFM ordering. The effective magnetic moment is approximately half of the expected moment (5.92μ_B) for the high spin Fe^{3+} (S=5/2) state. This is consistent with the fact that there is 50% to 45% dilution of the magnetic sublattice due to the presence of nonmagnetic Nb^{5+} ions. The low value of the effective moment may also be due to the presence of AFM clusters above T_N. To capture the atomic moments of Fe^{3+} in the paramagnetic state, one has to go to still higher temperatures to destroy such AFM clusters.

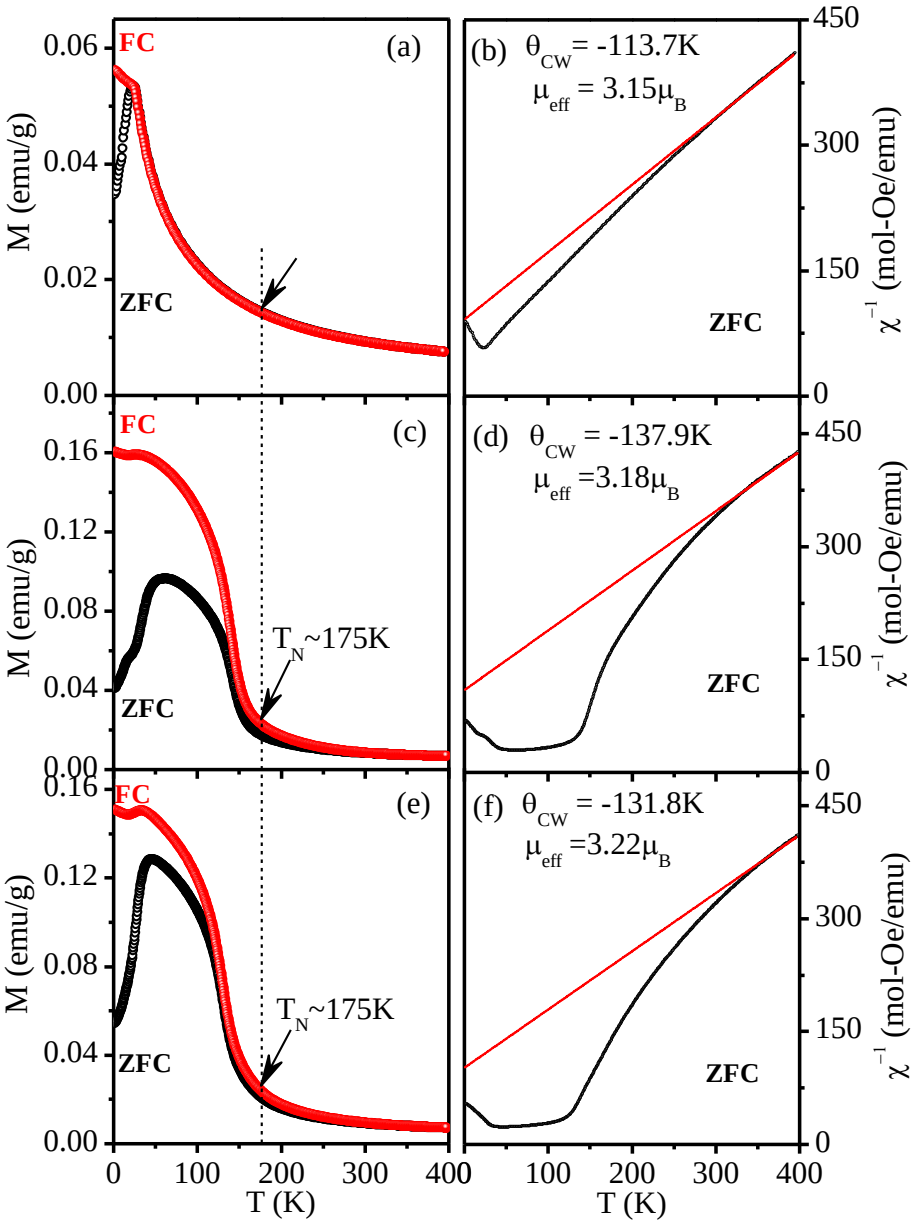

Figure 6.3: Left panel (a, c, e) depicts the ZFC and FC dc magnetization versus temperature plots for CFN, CFN-0.10BF and CFN-0.10LF, respectively and right panel (b, d, f) shows the corresponding Curie-Weiss plot using ZFC M(T) data.

6.4.3.2 Confirmation of LRO AFM state in CFN-0.10BF and CFN-0.10LF by neutron powder diffraction studies:

The LRO AFM nature of CFN-0.10BF and CFN-0.10LF below T_N~175K was confirmed by neutron scattering studies of the powder samples. Figs. 6.4 and 6.5 depict

the temperature evolution of the neutron powder diffraction (NPD) patterns of CFN-0.10BF and CFN-0.10LF in the temperature range 3-290K over a limited 2θ range of 5-70º. It is evident from the temperature evolution of the NPD patterns of both the solid solutions that a magnetic peak appears at 2θ = 19.04º corresponding to the **k** = ½½½ position of the AFM peak in the elementary perovskite unit cell. At room temperature, the peak is very broad indicating the presence of short-range ordered (SRO) AFM spin clusters even above T_N~175K. With decreasing temperature, the peak gets sharper. One may also notice a sudden increase in the peak intensity of this peak at T≲T_N ~175K revealing the growth of SRO AFM spin clusters into LRO AFM phase. This is in perfect agreement with the dc magnetization measurements of both the solid solution which show sudden increase in M(T) around 175K. It was verified that the nuclear structure does not change down to the lowest temperature of measurement (3K) as the two systems undergo an AFM phase transition. All the nuclear structure peaks in Figs. 6.4 and 6.5 are well indexed with respect to the unit cell of the Pbnm space group of CFN. Further, the observation of the 311, 310 and 021 peaks of ooo, ooe and oee type at 2θ = 36.88º, 35.16º and 24.52º, respectively, confirms the presence of anti-phase tilt, in-phase tilt and antiparallel displacement of Ca/Bi as well as Ca/La as expected for the $a^-a^-c^+$ tilt system in Glazer's notation [204]. The 311, 310 and 021 indices for the superlattice peaks are with respect to a doubled pseudocubic perovskite cell. Since the nuclear unit cell is already doubled, the AFM peaks corresponds to the propagation vector **k** = (0, 0, 0) of the doubled pseudocubic unit cell. It would correspond to **k** =½½½ position of AFM structure with respect to the elementary perovskite cell.

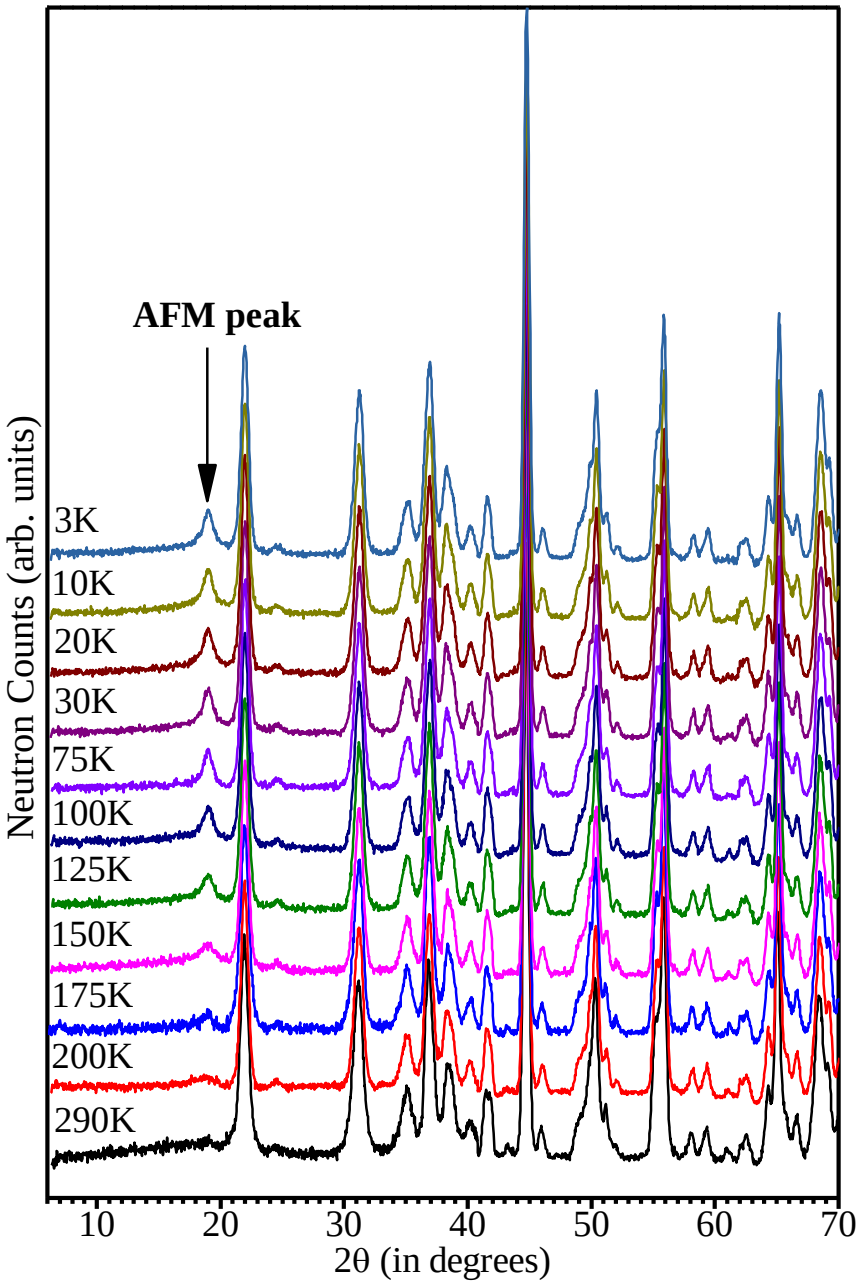

Figure 6.4: Temperature dependent evolution of NPD patterns of CFN-10BF over a limited 2θ range 5 to 70 degrees. Arrow marks the antiferromagnetic (AFM) ordering peak.

The magnetic peaks in the NPD patterns were indexed by considering additional phase in the refinement with propagation vector **k** = (0,0,0). We use representation theory approach to determine the magnetic structure of both the solid solutions below T_N ~175K. In the Pbnm space group, the list of irreducible representations corresponding to

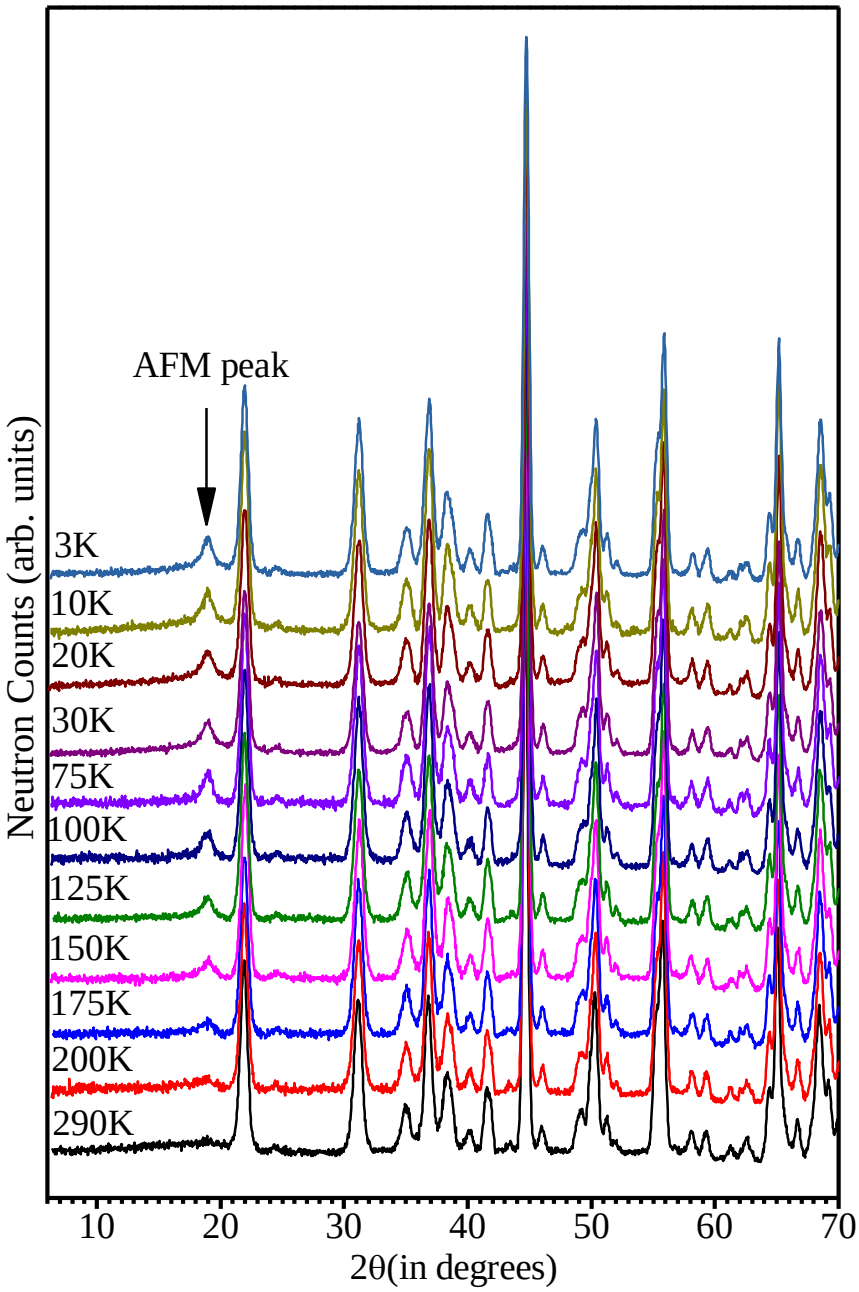

Figure 6.5: Temperature dependent evolution of NPD patterns of CFN-0.10LF over a limited 2θ range 5 to 70 degrees. Arrow marked the antiferromagnetic (AFM) ordering peak.

propagation vector **k** = (0,0,0) are Γ_1, Γ_2, Γ_3, Γ_4, Γ_5, Γ_6, Γ_7 and, Γ_8. All these irreps are one dimensional. In the orthorhombic unit cell with Pbnm space group, the magnetic ions Fe^{3+} occupy the 4b Wyckoff site with coordinates (1/2, 0, 0). As the Wyckoff position 4b contains a centre of symmetry, four of the above irreps, i.e. Γ_2, Γ_4, Γ_6, Γ_8, are not

allowed [319]. The magnetic reducible representation for the magnetic Fe^{3+} at the 4b site can therefore be decomposed as a direct sum of the irreducible representations as follows:

$$\Gamma(4b) = 3\Gamma_1 \oplus 3\Gamma_3 \oplus 3\Gamma_5 \oplus 3\Gamma_7 \quad \ldots\ldots\ldots (6.1)$$

The basis vectors associated with each irreducible representation are given in Table 6.3. All the four irreducible representations were considered in the Rietveld refinement of CFN-0.10BF to determine which irrep would give the best fit. The initial input parameters for Rietveld refinement of nuclear structure were taken from the Rietveld refinement using XRD data. The magnetic structure was considered as a second phase in the P-1 space group. Use of this space group in conjunction with representation theory

Table 6.3: The basis vectors of the irreducible representations of the space group Pbnm appearing in the magnetic representation at the Wyckoff position 4b for the wave vector k = (0, 0, 0).

IRs	Fe (4b)				
	Basis vectors	(x,y,z)	(-x,-y,z+1/2)	(x+1/2,-y+1/2,-z)	(-x+1/2,y+1/2,-z+1/2)
Γ_1	Ψ_1	(1 0 0)	(-1 0 0)	(1 0 0)	(-1 0 0)
	Ψ_2	(0 1 0)	(0 -1 0)	(0 -1 0)	(0 1 0)
	Ψ_3	(0 0 1)	(0 0 1)	(0 0 -1)	(0 0 -1)
Γ_3	Ψ_1	(1 0 0)	(-1 0 0)	(-1 0 0)	(1 0 0)
	Ψ_2	(0 1 0)	(0 -1 0)	(0 1 0)	(0 -1 0)
	Ψ_3	(0 0 1)	(0 0 1)	(0 0 1)	(0 0 1)
Γ_5	Ψ_1	(1 0 0)	(1 0 0)	(1 0 0)	(1 0 0)
	Ψ_2	(0 1 0)	(0 1 0)	(0 -1 0)	(0 -1 0)
	Ψ_3	(0 0 1)	(0 0 -1)	(0 0 -1)	(0 0 1)
Γ_7	Ψ_1	(1 0 0)	(1 0 0)	(-1 0 0)	(-1 0 0)
	Ψ_2	(0 1 0)	(0 1 0)	(0 1 0)	(0 1 0)
	Ψ_3	(0 0 1)	(0 0 -1)	(0 0 1)	(0 0 -1)

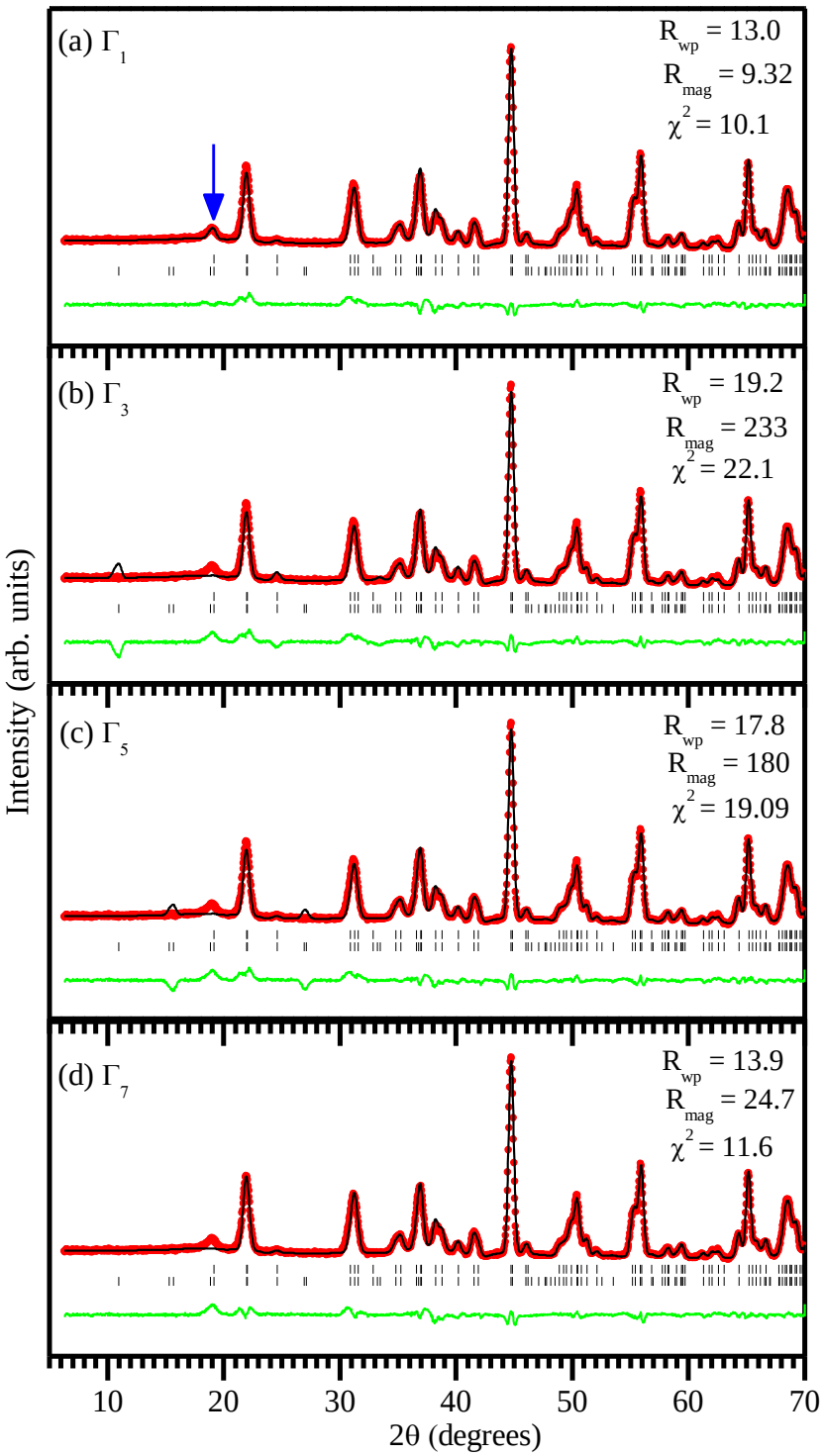

Figure 6.6: Observed (filled circles), calculated (continuous line), and difference (bottom line) profiles obtained from Rietveld refinement using NPD data of CFN-0.10BF at 100K for propagation vector k = (0,0,0) and the irreducible representations (a) Γ_1 (b) Γ_3 (c) Γ_5 and (d) Γ_7. Arrow marked the AFM peak. The vertical tick marks correspond to the position of all allowed Bragg reflections for the nuclear (top) and magnetic (bottom) reflections.

approach in FULLPROF package generates many fictitious magnetic peak positions also. Both the nuclear and magnetic structures were refined, and the refinement converged successfully after a few cycles. Figs. 6.6(a-d) compare the fits between the observed (filled-circles) and calculated (continuous line) profiles of CFN-0.10BF corresponding to the four irreps. It is evident from the figure that the irreps Γ_3, Γ_5 and Γ_7 fail to model the observed magnetic peak and therefore these irreps were rejected. The magnetic peak is well accounted by the irrep Γ_1. Hence, the irreducible representation Γ_1 represents the correct magnetic structure of CFN-0.10BF. A schematic depiction of the spin arrangement corresponding to the four irreps are shown in Fig. 6.7.

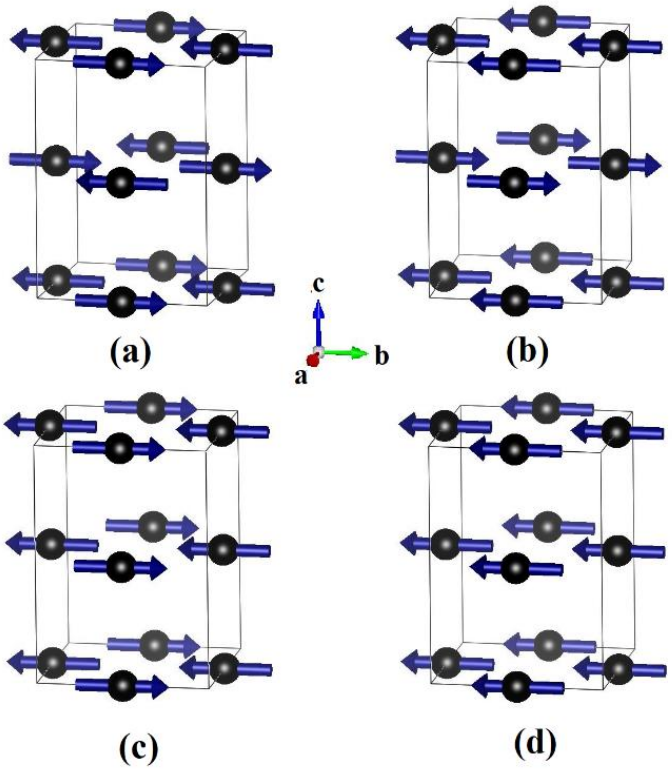

Figure 6.7: The magnetic structure of 0.90CFN-0.10BF corresponding to representation (a) Γ_1 (G-type AFM ordering) (b) Γ_3 (A-type AFM ordering) (c) Γ_5 (C-type AFM ordering) and (d) Γ_7 (FM-type Ordering).

In a similar way, we refined the magnetic structure of CFN-0.10BF and CFN-10LF solid solutions using the irreducible representation Γ_1 using the NPD pattern at 100K. Figs. 6.8 (a) and (b) show the results of the Rietveld refinements of CFN-0.10BF and CFN-0.10LF at 100K using Pbnm space group and magnetic structure corresponding to the irrep Γ_3. It can be clearly seen from the figures that the fit between the observed and calculated profiles is very good corresponding to the irrep Γ_1 which leads to G-type AFM

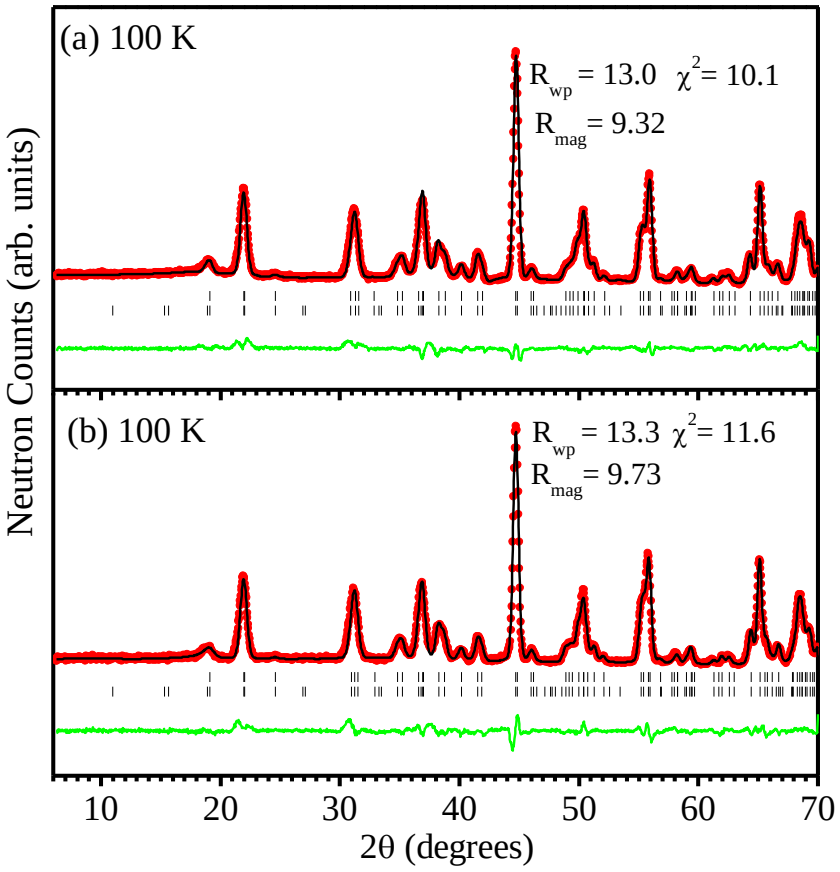

Figure 6.8: Observed (filled circles), calculated (continuous line), and difference (bottom line) profiles obtained from Rietveld refinement using NPD data at 100K for (a) CFN-0.10BF and (b) CFN-0.10LF for propagation vector k = (0,0,0) and the irreducible representation Γ_1. The vertical tick marks correspond to the position of all allowed Bragg reflections for the nuclear (top) and magnetic (bottom) reflections.

ordering as shown in Fig. 6.7(a). The refined lattice parameters, positional coordinates, thermal parameters and magnetic moment are listed in Table 6.4.

Table 6.4: Rietveld refined structural parameters and agreement factors for CFN-0.10BF and CFN-0.10LF using NPD data at 100K.

Parameters	**CFN-0.10BF**	**CFN-0.10LF**
$A_{O\,(Å)}$	5.4460 (2)	5.4566 (3)
$B_{O\,(Å}$	5.5589 (3)	5.5556 (2)
$C_{O\,(Å}$	7.7635 (4)	7.7705 (4)
α, β, γ	$\alpha=\beta=\gamma=90^0$	$\alpha=\beta=\gamma=90^0$
Ca/Bi (x)	0.006 (3)	0.005 (7)
Ca/Bi (y)	0.046 (3)	0.037 (3)
Ca/Bi (z)	0.25	0.25
Fe/Nb (x)	0.5	0.5
Fe/Nb (y)	0	0
Fe/Nb (z)	0	0
O1 (x)	0.9176 (1)	0.9128 (2)
O1 (y)	0.4758 (9)	0.473 (1)
O1 (z)	0.25	0.25
O2 (x)	0.2946 (1)	0.2932 (9)
O2 (y)	0.2958 (3)	0.2987 (3)
O2 (z)	0.0452 (5)	0.045 (1)
$\beta_{Ca/Bi}$ (Å^2)	1.24 (2)	1.31 (6)
$\beta_{Fe/Nb}$ (Å^2)	0.59 (4)	0.73 (2)
β_{O1} (Å^2)	0.52 (2)	0.68 (5)
β_{O2} (Å^2)	0.71(5)	0.89 (4)
$\mu Fe\,(\mu_B)$	3.09	2.97
R_{wp} (%)	13.0	13.3
R_{mag} (%)	9.32	9.73
χ^2	10.1	11.6

It is interesting to note that both $BiFeO_3$ and $LaFeO_3$ substitutions stabilize the LRO AFM phase with T_N~175K. This raises doubts about the earlier proposition [175] that the absence of LRO AFM phase in Pb-free $A(Fe_{1/2}B_{1/2})O_3$ systems is due to the absence of $6s^2$ lone pair electrons of Pb^{2+} in Ca^{2+}, Sr^{2+} and Ba^{2+}. We deliberately chose $LaFeO_3$ substitution to rule out the possible role of $6s^2$ lone pair electrons of Bi^{3+} in the CFN-0.10BF system. La^{3+} has no such lone pair, whereas both CFN-0.10BF and CFN-0.10LF exhibit LRO AFM transition with T_N~175K. Thus the stabilization of the LRO AFM state is due to the increase in the concentration of Fe^{3+} ion by 5% in the magnetic

sublattice, which, we believe, enabled crossing the percolation threshold value for both the solid solution systems to exhibit LRO AFM state.

6.4.4 Evidence for incipient-AFM nature of CFN:

In order to obtain insight into the possible reason for the stabilization of the LRO AFM as a result of 10% $BiFeO_3$/ $LaFeO_3$ substitution in CFN, we carried out a careful study of CFN itself. The basic idea was to verify if there is any anomaly occurring around T_N~175K in CFN also. We present the results of NPD and dielectric studies in this section to show that CFN is an incipient AFM and is at the verge of acquiring LRO AFM state.

6.4.4.1 Temperature dependent neutron powder diffraction studies:

We have carried out NPD measurements on CFN to explore the growth of local AFM SRO clusters, already mentioned in the previous chapter. Fig. 6.9(a) depicts the temperature evolution of the NPD patterns of CFN in the 300K-4K range over a limited 2θ region 13 to 50º at 25K interval. It can be clearly seen from the figure that magnetic Bragg peaks showing LRO AFM state are not present in the NPD patterns down to 4 K. However, a broad diffuse peak is seen at the AFM peak position (see Fig. 6.9(b)). This broad peak arises due to magnetic diffuse scattering as a result of the development of the short-range antiferromagnetic AFM correlations as discussed in the previous chapter. The evolution of the magnetic diffuse scattering as a function of temperature shown in Fig. 6.9(b) reveal that the broad diffuse peak due to short-range AFM ordering becomes sharper. This indicates that the short-range AFM correlation length increases with decreasing temperature. To determine the magnetic correlation length (ξ) of the AFM spin clusters using Scherrer formula ($\xi = 0.9\lambda/\beta\cos\theta$), we first deconvoluted the diffuse magnetic peak along with two neighbouring peaks to determine the FWHM of the diffuse

peak using three Gaussian functions, as explained in the preceding chapter. The deconvoluted patterns of the diffuse magnetic peak at two selected temperatures 250K and 100K are shown in Figs. 6.10(a) and (b). The FWHM (β) of the diffuse magnetic peak was further corrected for the instrumental broadening as in the preceding chapter. The temperature variation of correlation length ξ, obtained from the intrinsic FWHM of the diffuse peak, is shown in Fig. 6.11.

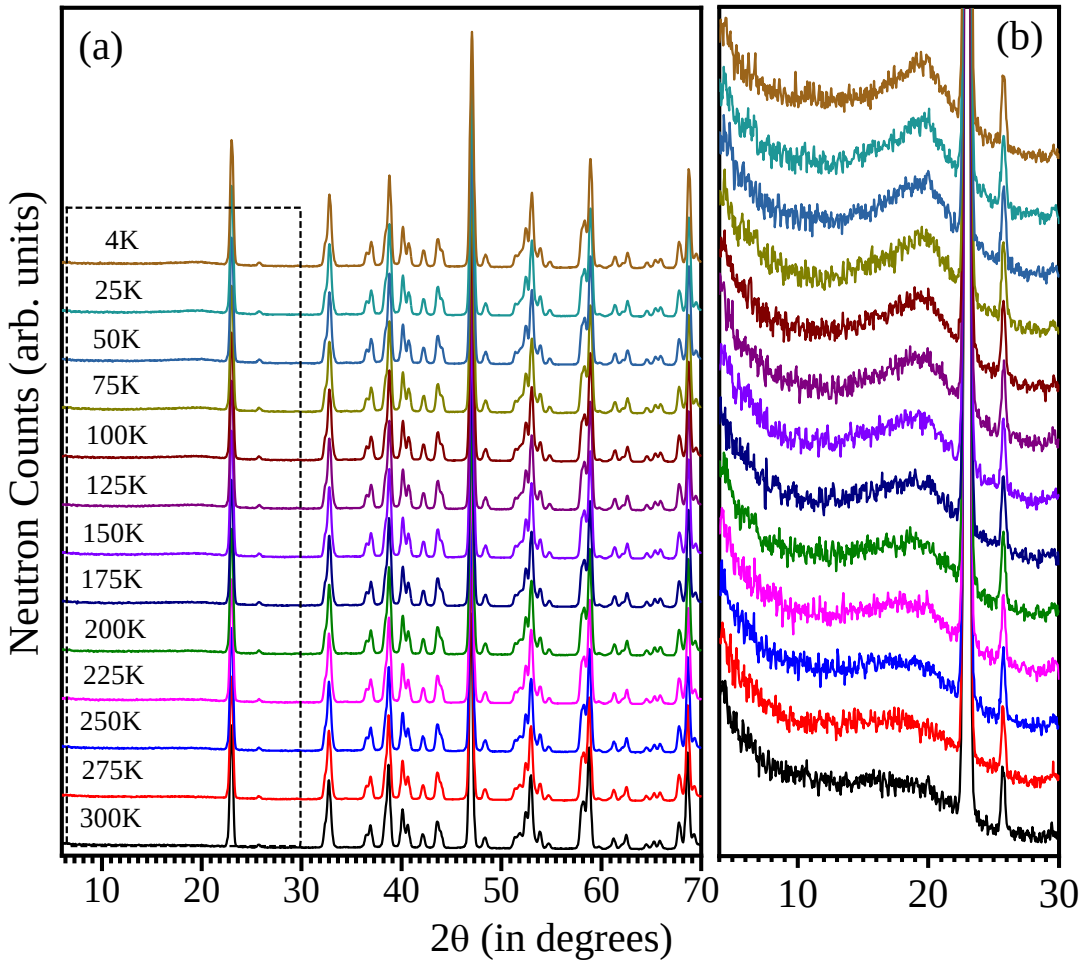

Figure 6.9: (a) Temperature evolution of NPD patterns of $Ca(Fe_{1/2}Nb_{1/2})O_3$ in the 4 to 300K range and (b) shows the temperature evolution of diffuse magnetic peak on a magnified scale.

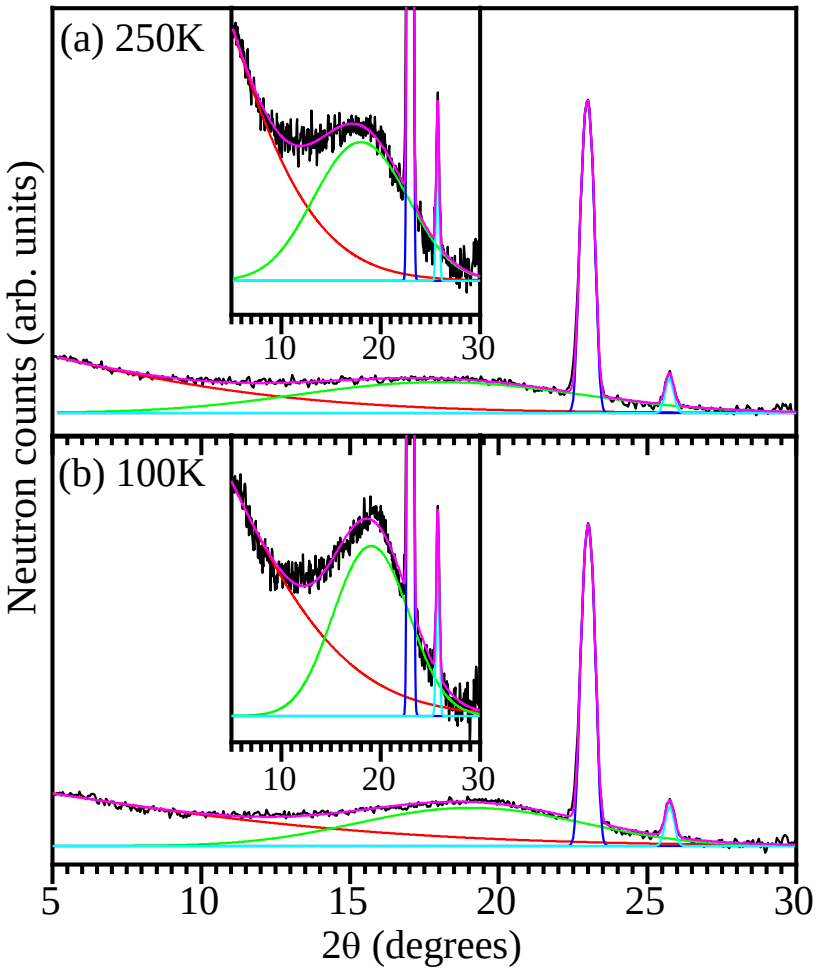

Figure 6.10: (a) Shows the deconvoluted peak profiles for diffuse magnetic peak using Gaussian function at (a) 250K and (b) 100K for CFN. Insets depict the magnetic diffuse peak on a magnified scale.

It is evident from the figure that the AFM correlation length ξ is nearly constant up to ~200K but starts growing gradually with decreasing temperature down to 4K ((~20Å). This suggests that the short-range ordered AFM correlations have a tendency to grow further below~200K. However, the correlation length grows very slowly and does not show any sharp divergence expected for a LRO transition down to 4K. On the contrary, the largest correlation length corresponding to 4K is still <2nm. This shows that

while CFN is at the verge of a criticality below 200K, the AFM interactions are highly restricted and are not able to stabilize the LRO AFM phase in CFN.

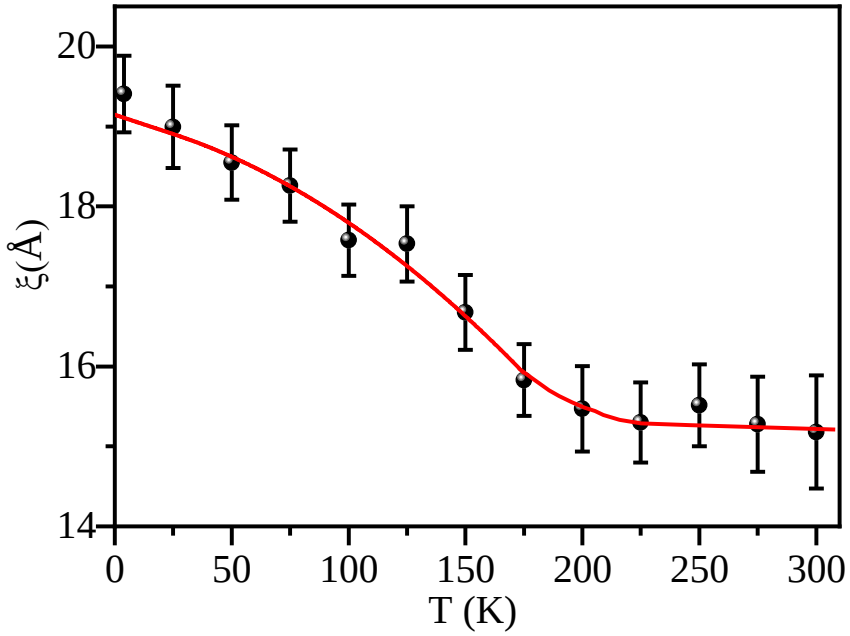

Figure 6.11: Variation of correlation length (ξ) with temperature for CFN.

6.4.4.2 Evidence for magnetoelastic and magnetodielectric couplings around 160 to 175K:

It is evident from the qualitative inspection of the NPD profiles of CFN shown in Fig. 6.9(a) that no new peaks appear/disappear in the 4 to 300K temperature range. As pointed out in the previous chapter, the room temperature crystal structure of CFN corresponds to orthorhombic Pbnm space group with $a^-a^-c^+$ tilt system. The absence of any structural transition below 300K was further confirmed by the Rietveld refinements using the NPD data after excluding the diffuse magnetic peak. Fig. 6.12 depicts the fits obtained between the observed and calculated profiles obtained by Rietveld refinement of CFN at a few selected temperatures. The observed and calculated profiles show excellent fit at all temperatures as can be seen from the difference profile shown at the bottom of the figure.

The temperature dependence of the unit cell parameters A_o, B_o, C_0 and unit cell volume (V_o) of the CFN, as obtained from Rietveld refinements, is shown in Figs. 6.13 (a) (b), (c) and (d), respectively. It is evident from this figure that the lattice parameter A_o and C_o show usual thermal expansion behaviour whereas the lattice parameter B_o shows a dip around 175K. This anomaly in the B_0 parameter correlates with the temperature at which the correlation length of the AFM spin clusters starts growing, as can be seen from a comparison of Fig. 6.13 (b) with Fig. 6.11. We believe that the growth of SRO AFM clusters is accompanied with magnetoelastic coupling which gives rise to this anomalous dip in B_0 lattice parameter around 175K.

To capture the signature of magnetoelastic coupling, we modelled the unit cell volume of CFN using Debye-Grüneisen equation given by [264]:

$$V \cong V(0) + \frac{9\gamma N k_B}{B} T \left(\frac{T}{\Theta_D}\right)^3 \int_0^{\Theta_D/T} \frac{x^3}{e^x - 1} dx, \qquad \text{……..(6.2)}$$

where V(0), γ, B and Θ_D are unit cell volume at 0K, Grüneisen parameter, bulk modulus, and Debye temperature, respectively. A least square fit to the observed unit cell volume in the temperature range 200K≤T≤300K gives the value of V(0), Θ_D, and C (=9γNk_B/B) as (233.313±0.005) $Å^3$, (612 ± 5) K and (0.0266±0.0002)$Å^3$/K, respectively. The best fit curve is shown as a continuous line in Fig 6.13 (d). It can be clearly seen from the figure that the observed unit cell volume starts deviating from the Debye-Grüneisen curve at T≲175K revealing an excess volume (ΔV) over the phonon contribution. We have plotted volume strain ΔV/V versus M^2 (obtained from DC M(T) data at 1T field) which shows linear dependence in the temperature range 125-175K (see inset of Fig. 6.13). The quadratic dependence of the excess volume on magnetization suggests the appearance of magnetoelastic coupling at T≃175K.

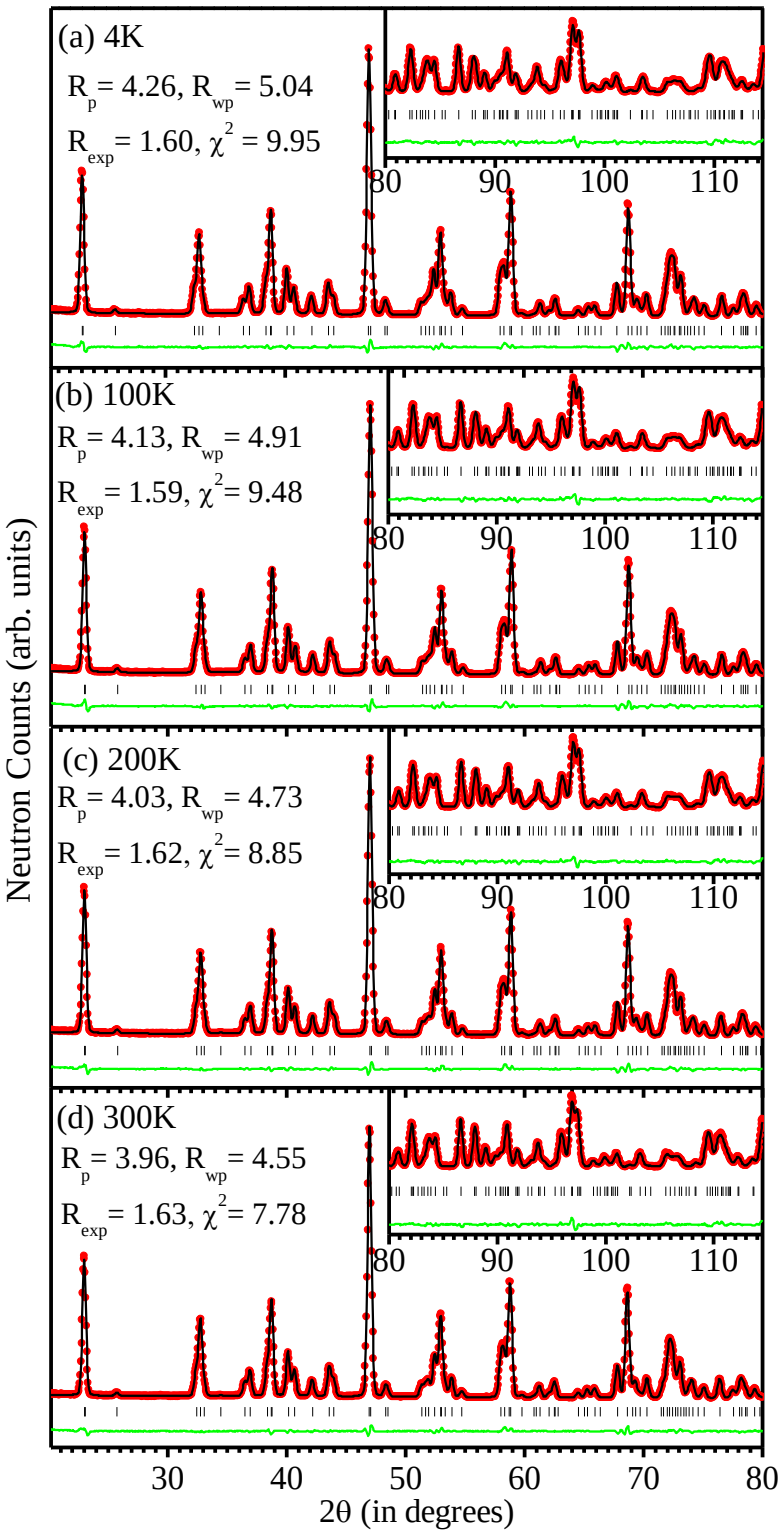

Figure 6.12: (a to d) Observed (red dots), calculated (black continuous line) and difference (green continuous line) profiles obtained from Rietveld refinement using NPD patterns of $Ca(Fe_{1/2}Nb_{1/2})O_3$ at 4K,100K 200K and 300K, respectively, for Pbnm space group. Vertical tick marks above the difference profile represent the Bragg peak positions. Here, we have excluded the magnetic diffuse scattering region on the refinement.

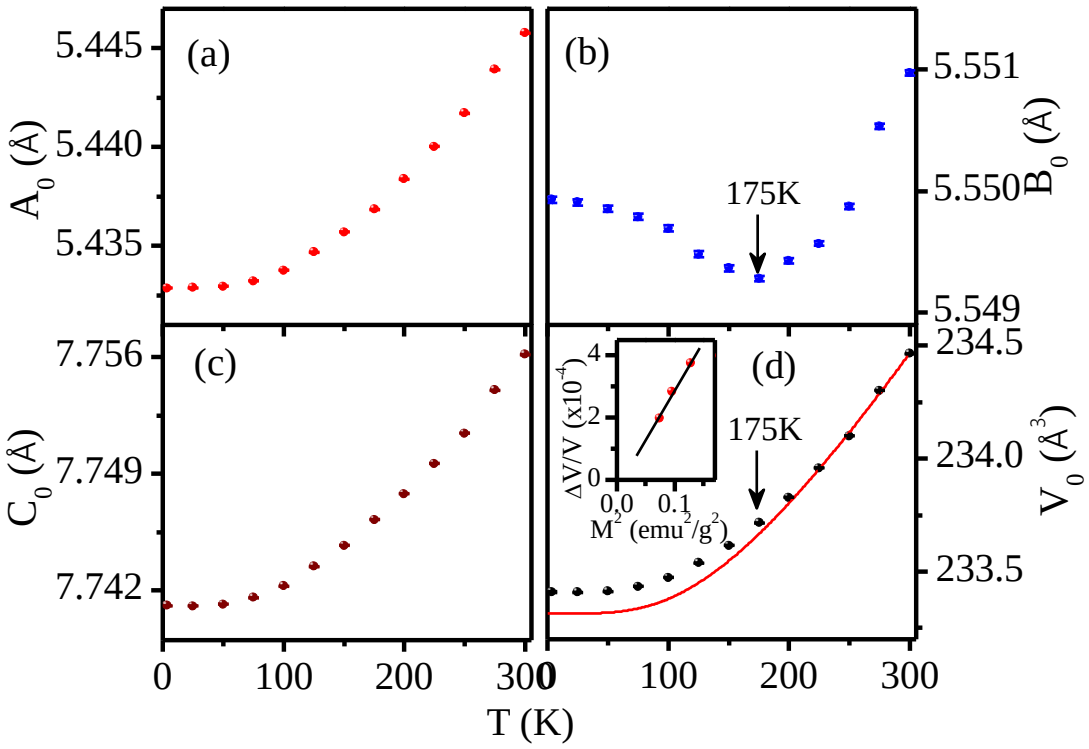

Figure 6.13: Temperature variation of lattice parameters (a to c) and unit cell volume (d) of $Ca(Fe_{1/2}Nb_{1/2})O_3$ obtained from Rietveld refinement using NPD patterns.

We have also calculated the in-phase and anti-phase tilt angles φ and γ using following relationships for the $a^-a^-c^+$ tilt system [320]:

$$tan\varphi = \frac{4zC_o}{\sqrt{[(A_o)^2+(B_o)^2\,]}}\text{, and} \qquad \text{…….(6.3)}$$

$$tan\gamma = 4\left[\frac{\{(xA_o)^2+(yB_o)^2\}}{(A_o)^2+(B_o)^2}\right]^{\left(\frac{1}{2}\right)} \qquad \text{……..(6.4)}$$

where A_o, B_o and C_o are the lattice parameters of the orthorhombic cell and x, y and z, are positional coordinates of oxygen atom O_{II} at the 8d Wyckoff position. To calculate the in-phase (φ) and anti-phase (γ) tilt angles, we have used unit cell parameters and positional coordinates obtained from NPD data by Rietveld refinement at various temperatures in the range 4 to 300K. The temperature variation of both the tilt angles are shown in Fig. 6.14. It is evident from the figure that distinct anomalies occur not only at T~175K but also at the spin glass freezing temperature $T_f \simeq 25K$. As mentioned earlier, tilting of the

oxygen octahedra bends the Fe^{3+}-O^{2-}-Fe^{3+} bonds and makes the bond angle to deviate from ideal 180° in the cubic perovskite structure. As a result of such a bending of the Fe^{3+}-O^{2-}-Fe^{3+} bonds, the Dzyloshinkii-Moriya (D-M) interaction becomes non-zero and leads to spin canting. The Hamiltonian for the spin-spin interaction is written as [40]:

$$H_{D\text{-}M} = \sum_{ij}[J_{i,j}\,\mathbf{S}_i.\mathbf{S}_j + \mathbf{D}_{ij}.(\mathbf{S}_i \times \mathbf{S}_j)] \qquad \ldots\ldots(6.5)$$

Here, $J_{i,j}$ is the superexchange interaction between the nearest neighbour spins, i and j are the site indices, and **S** are spin vectors, D_{ij} is the D-M vector. Since the D-M interaction is a consequence of the spin-orbit (lattice/phonon) coupling which is reflected through the dip in the B_0 lattice parameter at T≃175K (see Fig. 6.13(b)), the dip in the B_0 parameter and the tilt angles at T≃175K seem to correlate with each other and lead to possible spin canting through D-M interaction term.

The temperature dependence of the real part of the dielectric constant (ε') of CFN in the range 4-300K measured at 100kHz is shown in Fig. 6.15. It is evident from the inset to Fig. 6.15 that the real part of dielectric constant reveals a step jump around 160K, while no such anomaly/jump is observed across the spin-glass freezing temperature T_f≃25K. A similar step jump in the dielectric constant across the AFM transition has been reported in PFN at the Néel temperature T_N~150K [194] and explained in terms of magnetoelectric/magnetodielectric couplings. We believe that the step jump in the dielectric constant of CFN around 160K is also due to magnetodielectric coupling. The gradual increase in the AFM correlation length at T≲175K clearly suggests that the growth of AFM cluster size has magnetoelectric character giving rise to magnetodielectric effect shown in Fig. 6.15. The reason why the step jump in the dielectric constant occurs around 160K whereas the AFM correlation length ξ starts growing 175K is possibly because the neutron measurements were made at 25K interval

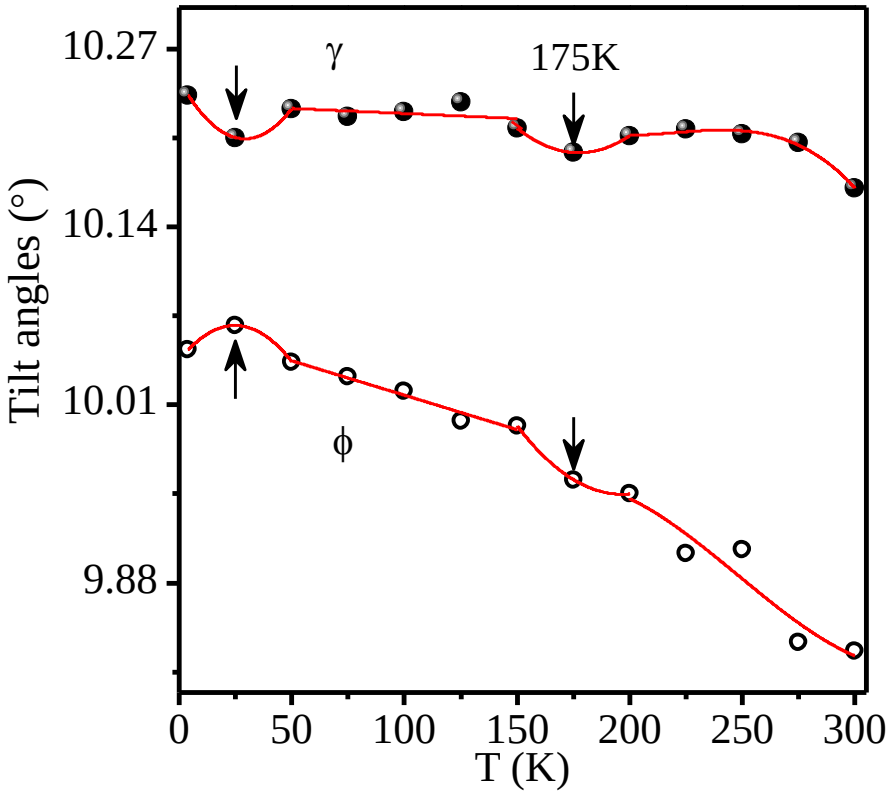

Figure 6.14: Temperature variation of in-phase (φ) and antiphase (γ) tilt angles of CFN.

whereas the dielectric data was collected at 3K interval. The dip around 175K may correspond to any temperature in the range 150K<T<200K. To locate the exact temperature, one needs NPD data at finer temperature intervals. Since the dielectric constant measurement was done at 3K interval, it gives more accurate value of the critical temperature below which CFN would show an anomalous growth of ξ accompanied with magnetoelastic and magnetodielectric couplings. All these results indicate that CFN ia at the verge of transforming into an LRO AFM, but since the concentration of magnetic spins in the magnetic sublattice is below the critical percolation threshold value, the LRO transition does not occur at T_N~175K. our results thus show that CFN is an incipient AFM and just 10% substitution by $BiFeO_3$ or $LaFeO_3$ in CFN is sufficient to stabilize LRO AFM state below this critical temperature T_N~175K.

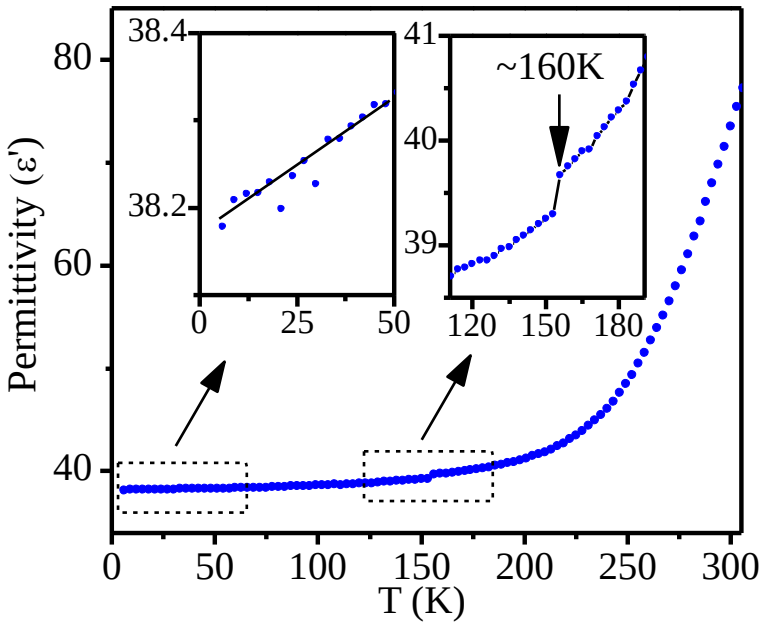

Figure 6.15: Shows the temperature dependence of dielectric permittivity (ε') of CFN. Insets depict the magnified scale across the AFM and SG transitions.

6.5. Conclusions:

We presented results of dc magnetization and neutron scattering measurements on CFN as well as CFN-0.10BF and CFN-0.10LF solid solutions. Our results reveal that CFN is an incipient AFM whose SRO AFM correlation length starts growing at T≲175K eventhough the size of the AFM spin-clusters remains limited to ~2 nm at the lowest temperature (4K). We showed that CFN is at the verge of acquiring LRO AFM state below T_N~175K if the Fe^{3+} content can be slightly increased by about 5% through a substitution of $BiFeO_3$ and $LaFeO_3$. We have also presented evidence for significant magnetoelastic and magnetodielectric coupling below T≲175K in CFN suggesting that CFN could become a multiferroic through suitable compositional engineering. More work, however, is needed to capture the signatures of ferroelectric distortion, even if it is at the local scale in CFN and its solid solutions with $BiFeO_3$ and $LaFeO_3$, through atomic pair distribution function analysis.